Analysis of Near-Source Ground Motion from the 2019 Ridgecrest Earthquake Sequence

Georgios Baltzopoulos[*1], Lucia Luzi[2], and Iunio Iervolino[1]

ABSTRACT

The Ridgecrest seismic sequence began on 4 July 2019 in California, on a hitherto relatively unmapped orthogonal cross-faulting system, causing mainly nonstructural or liquefaction-related damage to buildings in the vicinity of Ridgecrest and Trona, and also causing substantial surface rupture. The present study considers the near-source ground-acceleration recordings collected during the two principal events of the sequence—the 4 July moment-magnitude M 6.4 foreshock and the 6 July M 7.1 mainshock—to identify pulse-like ground motions, which may have arisen due to forward rupture directivity. Pulse-like seismic input is of particular interest to earthquake engineering due to its peculiar spectral shape and possibly increased damaging potential, and expanding the strong-motion databases with such records is a topical issue. In this context, a pulse identification methodology is implemented, partially based on computer-aided signal processing, but also involving manual classification. Nine ground-motion records were classified as pulse-like by this procedure. Further investigation led to the conclusion that, for some of these records, the impulsive characteristics could most likely be attributable to forward rupture directivity, whereas for others fling step may have also been an issue. Finally, clear signs of directionality were observed in these ground motions at periods near the pulse duration, manifesting as a polarization of the spectral ordinates toward the orientation of the impulsive component.

KEY POINTS

- The near-source acceleration recordings obtained during the Ridgecrest sequence are analyzed.
- Pulse-like ground motions are identified and possible causal effects, including directivity, are discussed.
- Impulsive records exhibit directionality, with spectral ordinates around the pulse period being polarized.

Supplemental Material

INTRODUCTION

For a long time, engineering seismology has recognized that near-source acceleration records may deserve to be studied separately from those recorded farther away from the fault rupture (the latter often termed far-field ground motions). The main reason for this distinction was the fact that ground motions recorded near the ruptured fault appeared, on average, more potentially damaging to structures than far-field accelerograms of the same amplitude (Baez and Miranda, 2000). In fact, an early study that examined structural response to near-source records of the 1971 San Fernando (California) earthquake (Bertero *et al.*, 1978) was the first to incriminate the impulsive characteristics of some near-fault ground motions for the severity of the deformation demands they imposed on structures. At present, there is a wide consensus that the importance of near-source accelerograms for earthquake engineering is not just a matter of distance from the fault but, more importantly, an issue of occurrence (or not) of particular near-source effects. One of the most prominent near-source effects with engineering relevance is the occurrence of distinct velocity pulses in the ground motion.

The engineering significance of pulse-like records stems from the peculiar, narrowband amplification of both elastic and inelastic structural response that such ground motions exhibit; the main concern of earthquake engineers is the fact that, on average, pulse-like ground motions can subject ductile structures to greater inelastic displacements when compared to nonimpulsive seismic input (e.g., Alavi and Krawinkler, 2004; Baltzopoulos *et al.*, 2015). Several past studies suggest that the systematic differences in inelastic displacement demand between pulse-like and non-pulse-like, that is ordinary, records are directly related to the peculiar spectral shape of the former,

1. Università degli studi di Napoli Federico II, Dipartimento di Strutture per l'Ingegneria e l'Architettura, Naples, Italy; 2. Istituto Nazionale di Geofisica e Vulcanologia, Sezione di Milano, Milan, Italy

*Corresponding author: georgios.baltzopoulos@unina.it

Cite this article as Baltzopoulos, G., L. Luzi, and I. Iervolino (2020). Analysis of Near-Source Ground Motion from the 2019 Ridgecrest Earthquake Sequence, *Bull. Seismol. Soc. Am.* **XX**, 1–11, doi: 10.1785/0120200038

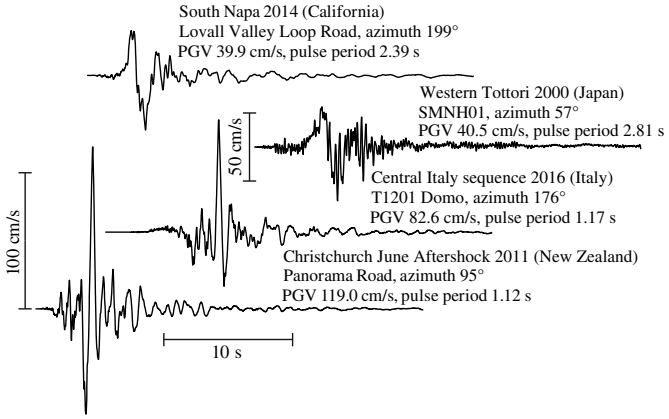

Figure 1. Pulse-like velocity traces recorded during earthquakes from California, Japan, Italy, and New Zealand. All traces drawn to common amplitude and time scales, with 30 s segments shown for each record. Recording station and rotated orientation of the trace reported under event names. PGV, peak ground velocity.

which is influenced by the presence of the pulse (e.g., Tothong and Cornell, 2008; Bojórquez and Iervolino, 2011).

Pulse-like ground motions may be the result of various phenomena, with the most notorious being forward rupture directivity. During fault rupture, shear dislocation typically propagates at velocities near the shear-wave velocity; this may cause seismic waves that were emitted at different points along the rupture front to arrive almost simultaneously at near-source sites aligned with the propagation path. In such cases of so-called forward directivity, the radiation pattern of the seismic source can lead to constructive wave interference that appears in the form of a double-sided velocity pulse (Somerville *et al.*, 1997). As an example, four such pulse-like ground-velocity traces are shown in Figure 1 (taken from the near-source strong-motion dataset; Pacor *et al.*, 2018—see Data and Resources). The conditions for the emergence of directivity may be particularly favorable in the proximity to asperities on the rupture plane (for some examples from recent events, see Iervolino *et al.*, 2016; Tinti *et al.*, 2016). Such a pulse contains most of the seismic energy concentrated early in the record. Other phenomena that may also give rise to pulse-like ground motions are fling step and basin or site effects. Fling step refers the static offset experienced by sites near the fault plane, which may be the result of either wave propagation generated from finite dislocation or the plastic response of near-surface materials (e.g., Boore and Bommer, 2005). The term fling step is due to the fact this static offset appears as a step in the ground displacement time series, which also results in a one-sided pulse appearing in the velocity trace (Bolt, 2010). On the other hand, wave-entrapment phenomena, observed at the edges of alluvial basins, may also produce constructive interference effects (e.g., Pitarka *et al.*, 1998), whereas site effects can result in narrowband signal amplification (e.g., Bradley and Cubrinovski, 2011; Luzi *et al.*, 2019). In both cases, these effects can result in monochromatic waveforms, with similar characteristics to directivity-induced pulse-like ground motions.

For any given seismic event, the observation of pulse-like ground motions is not guaranteed at all sites near the fault rupture; the probability of occurrence of this effect primarily depends on site-to-source geometry and focal mechanism (Iervolino and Cornell, 2008). For this reason, pulse-like records used to be a relative rarity in older ground-motion databases due to sparsity of near-source records, whereas more recent seismic events occurring amidst dense accelerometric networks tend to provide increasing numbers of such examples (e.g., Chioccarelli and Iervolino, 2010; Luzi *et al.*, 2017). In this spirit, the present work investigates the near-source ground accelerations recorded during the two main events of the 2019 Ridgecrest earthquake sequence in California. The principal events of the Ridgecrest sequence considered in this study are the moment magnitude **M** 6.4 event that occurred on 4 July 2019 and the subsequent **M** 7.1 event of 6 July 2019. Hereafter, these two events will be referred to as the foreshock and the mainshock of the sequence, respectively. Both ruptures occurred on predominantly strike-slip faults that were largely unmapped and oriented almost perpendicular to each other. This situation is referred to as a case of orthogonal cross-faulting and constitutes a phenomenon that is endemic to strike-slip structures of southern California, but has also been encountered elsewhere in the world (Barnhart *et al.*, 2019; Ross *et al.*, 2019). The mainshock caused mainly nonstructural or liquefaction-related damage to buildings in the vicinity of Ridgecrest and Trona and also substantial surface rupture (Stewart *et al.*, 2019; Hough *et al.*, 2020).

Thanks to a fairly dense accelerometric network deployed in the area between the town of Ridgecrest and Searles Lake, a large number of near-source ground-motion records became available from these events. This motivates the present study, the main goal of which is to analyze these near-source ground motions, identify those with potentially impulsive characteristics and perform a basic binary classification between pulse-like and ordinary motions. The remainder of the article is organized as follows: first, an overview of the available data is given, in terms of available acceleration records and finite-fault geometry models; then, the pulse classification methodology is illustrated and the results of its application to the ground-motion dataset, at hand, is given; finally, the results are discussed in terms of the impulsive features and their potential causes, and some concluding remarks are provided in the end.

IDENTIFICATION OF PULSE-LIKE GROUND MOTIONS IN THE RIDGECREST SEQUENCE

Near-source strong-motion records and finite-fault geometry

We investigate the horizontal acceleration components from 27 stations that recorded the **M** 7.1 mainshock having epicentral

distances between 3.3 and 80 km and 26 stations that recorded the **M** 6.4 foreshock with epicentral distances between 14 and 79 km. The raw ground-acceleration waveforms were obtained from the Southern California Seismic Network (Hutton *et al.*, 2010), the United States National Strong-Motion Network (U.S. Geological Survey [USGS] Earthquake Science Center, 1931) and the California Strong Motion Instrumentation Program (see Data and Resources). Manual processing of the raw acceleration data was performed according to the procedure described in Pacor *et al.* (2011). Velocity traces were obtained via integration of the corrected acceleration records.

For the purposes of this study, the finite-fault geometry models proposed by Liu *et al.* (2019) were adopted for the two events (see Data and Resources). It should be mentioned that only one alternative set of rupture models was already available in the literature at the time of this study (Ross *et al.*, 2019) and that the choice between them was made primarily on the basis of data availability. For the foreshock, the model entails two perpendicular fault segments forming an L-shape, with strikes of 227° and 316°, one dipping vertically and the other at an angle of 85°. For the mainshock, the proposed finite-fault geometry is composed by four vertically dipping segments, with strikes varying from 312° to 334°. According to this model, the mainshock rupture propagated bilaterally, and most of the slip was concentrated near the hypocenter, straddling the foreshock slip.

Pulse classification methodology

Various methods have been proposed in the literature for the quasi-automatic detection of pulse-like features among large databases of seismic waveforms. These include methodologies that use empirically calibrated quantitative criteria or indices, usually obtainable by manipulations of the ground-motion time series (e.g., Baker, 2007; Hayden *et al.*, 2014; Shahi and Baker, 2014a), methods that employ spectral-shape-based criteria (Tang and Zhang, 2011), and some that make classifications based on energy considerations (Zhai *et al.*, 2013). One feature that these methods have in common is that they all rely on information and parameters that are obtainable solely from the ground-motion record itself, to the exclusion of considerations related to source kinematics and the physical process of fault dislocation. Because of this, pulse-like features that are detected by these algorithms cannot always be attributed to forward rupture directivity or other specific source-related phenomena. This remains the case despite auxiliary criteria such as the distinction between early- and late-arriving pulses, with the former being considered as more likely to be caused by rupture directivity.

These methods have been tested and calibrated on ground-motion datasets of varying size and characteristics, but it is always hazardous to rely on a completely automated application of any single criterion upon a new database. In this spirit, a more prudent approach is adopted: that of parsing the available ground-motion records with the help of an automated algorithm and then proceeding with manual characterization with visual inspection of spectral and waveform shapes as an additional classification criterion. More specifically, the continuous wavelet transform algorithm proposed by Baker (2007) was applied to each two-horizontal-component ground-motion record, rotated over all nontrivial orientations spanning 180°, and the pulse indicator (PI) score was calculated according to

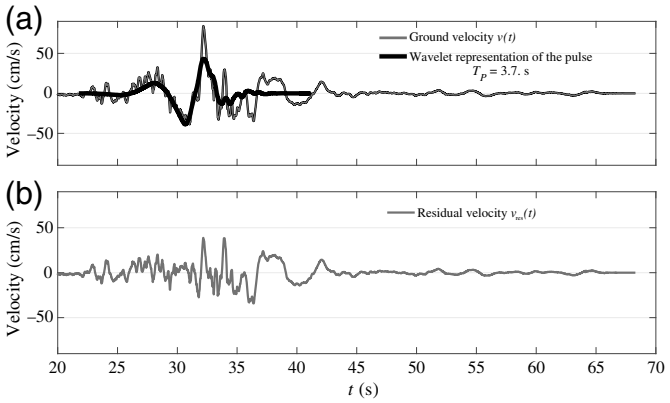

Figure 2. Original ground velocity, extracted wavelet representation of the (a) candidate pulse and (b) residual velocity resulting from application of Baker's wavelet transform-based algorithm to the Christmas Canyon China Lake record rotated at an azimuth of 47°.

$$\mathrm{PI} = \left[1 + \exp\left(-23.3 + 14.6 \cdot \frac{\max\{|v(t)|\}}{\max\{|v_{\mathrm{res}}(t)|\}} + 20.5 \cdot \frac{\int_{t_1}^{t_2} v^2(t) \cdot dt}{\int_{t_1}^{t_2} v_{\mathrm{res}}^2(t) \cdot dt}\right)\right]^{-1}, \quad (1)$$

in which $v(t)$ is the ground-velocity time history obtained from numerical integration of the corresponding rotated acceleration record, $v_{\mathrm{res}}(t)$ is the residual velocity remaining after the wavelet-based representation of the candidate pulse has been extracted from $v(t)$, $[t_1, t_2]$ defines the start–end time interval of the record. An example of original versus residual ground velocity is provided in Figure 2 for the Christmas Canyon China (CCC) Lake station record of the **M** 7.1 mainshock, which is found at a distance from the surface projection of rupture (or Joyner–Boore distance R_{JB}) of 2 km, rotated at an azimuth of 47°; in the figure, the pulse to be subtracted from $v(t)$ is shown, along with the resulting $v_{\mathrm{res}}(t)$. The pulse period (T_p) reported in the figure is an important parameter for earthquake engineering applications (e.g., Champion and Liel, 2012; Baltzopoulos *et al.*, 2015) and is defined here as the pseudo-period of the highest-energy constituent wavelet of the pulse. PI scores fall in the (0,1] interval; values near unity indicate that the most prominent local wavelet representation of the motion accounts for the majority of that motion's velocity amplitude and energy content, making that ground motion

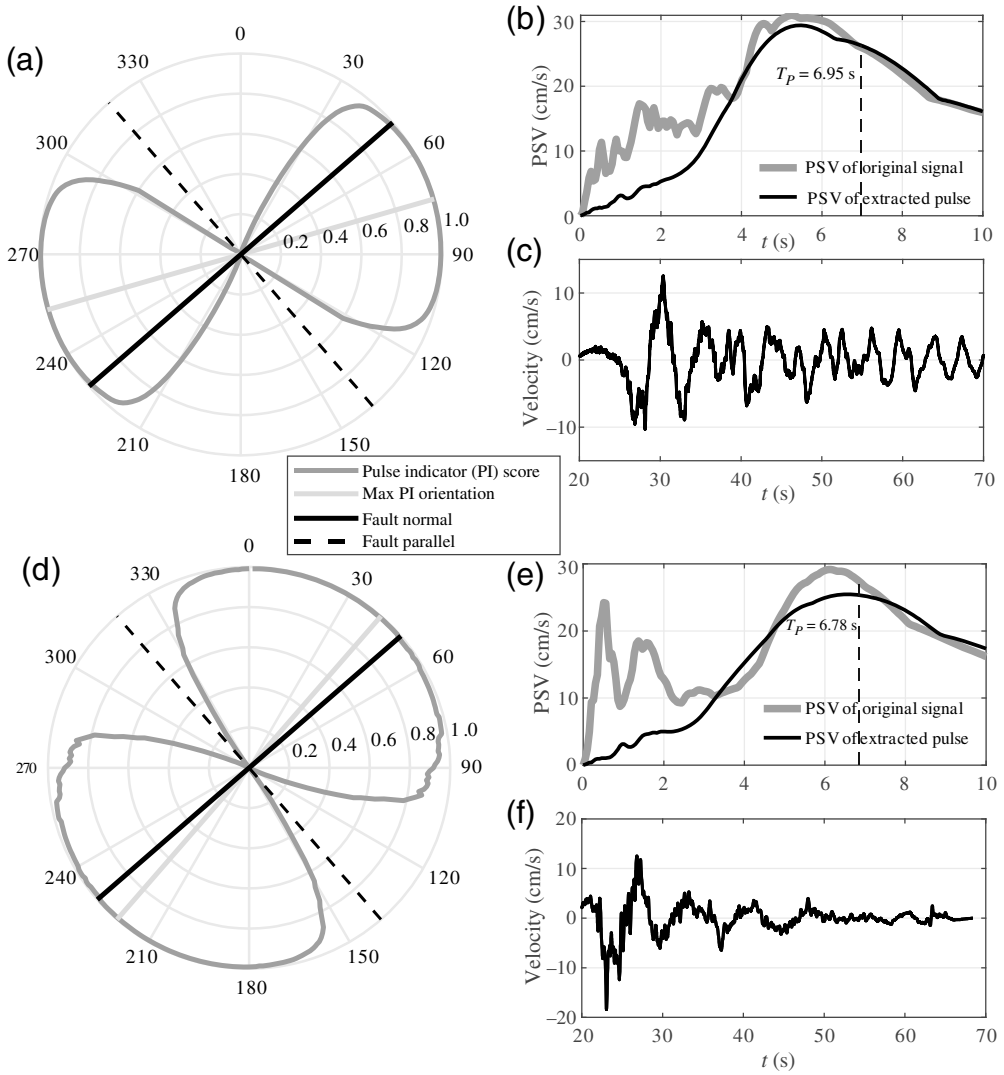

Figure 3. Polar plot of (a) pulse indicator (PI), (b) pseudovelocity spectrum (PSV) of the original signal against that of the extracted pulse, (c) velocity time series at the orientation exhibiting maximum PI for the mainshock record at station 43158, and (d–f) corresponding plots for the mainshock record at station WRV2.

a likely candidate for being classified as impulsive. On the other hand, a PI score near zero would suggest an ordinary ground motion, devoid of pulse-like characteristics.

According to the original algorithm, ground motions with PI ≥ 0.85 could be classified as pulse-like, whereas those with 0.15 ≤ PI < 0.85 fall in the ambiguous territory. Here, the algorithm is primarily employed as a first screening tool, so all cases with PI ≥ 0.50 are set apart for visual inspection and are classified as pulse-like on condition of meeting three additional criteria: (1) persistence of high PI values over a contiguous range of orientations spanning at least 30°, (2) good local fit of the pseudovelocity spectrum (PSV) of the extracted candidate pulse to the PSV shape of the original ground motion at natural vibration periods near and around T_p, and (3) maximum ground-velocity amplitude satisfying $\max\{|v(t)|\} \geq 10$ cm/s. Directivity pulses known from the literature have been observed to score consistently high over a relatively wide range of directions (e.g., Shahi and Baker, 2011), and thus the first additional criterion is meant to exclude ground motions that only score high over a limited arc. The second criterion borrows from the alternative spectrum-matching identification procedures in the literature and is an indication that the wavelet is capturing the dominant impulsive waveform in the record.

These criteria are illustrated in Figure 3, in which PI polar plots, PSV, and $v(t)$ graphs are provided for the ground motions recorded during the **M** 7.1 mainshock at the stations Olancha (43158) and Rose Valley Canyon Two (WRV2). On the polar plots, the fault-normal and fault-parallel orientations are also indicated; these correspond to a single assumed strike of 319°, which is the arithmetic mean of the strikes of the four fault segments reported by Liu *et al.* (2019). From that figure, it can be seen that both of these records meet the aforementioned criteria for classification as pulse-like.

Classification results

Overall, one out of the 26 foreshock records investigated was labeled pulse-like, whereas, for the mainshock, the corresponding numbers were eight impulsive motions out of 27 considered. In the latter case, there were also three ambiguous cases, some of which will be discussed later on. The spatial distribution of pulse-like and ordinary records around the finite-fault geometries of the two events is shown in Figure 4. If one only considers ground motions within $R_{JB} \leq 30$ km, these amount to one out of seven of the examined records exhibiting pulse-like characteristics for the foreshock and six out of 10 for the mainshock. Some basic information about the records classified as impulsive is summarized in Table 1, including pulse period, and whether or not the impulsive components are oriented toward the perpendicular to the strike of the fault,

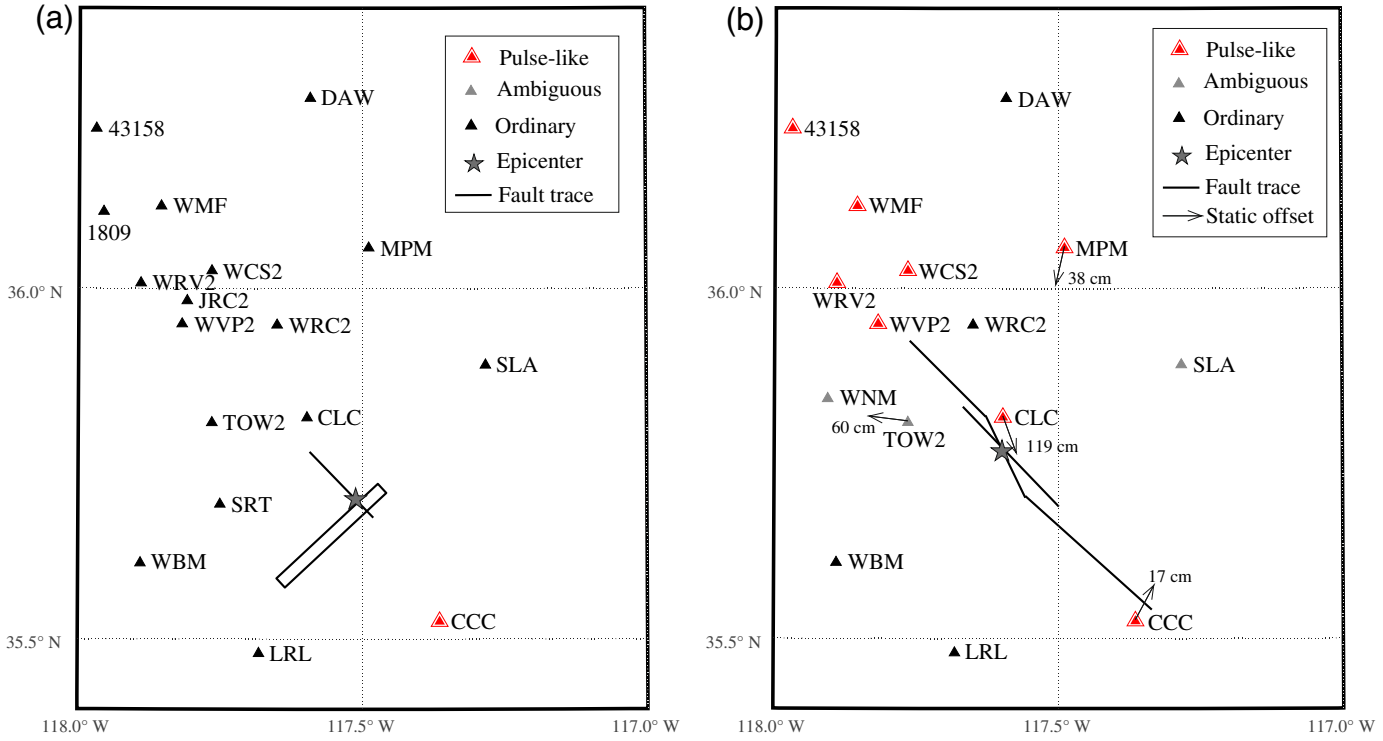

Figure 4. Accelerometric stations in which ordinary, pulse-like, and ambiguous ground motions were recorded, according to the classification performed, during the (a) M 6.4 foreshock and the (b) M 7.1 mainshock. Static offset horizontal displacements reported for the mainshock by Liu *et al.* (2019) are also shown at four stations, with an arrow indicating the direction and the displacement value reported by the arrowhead. The color version of this figure is available only in the electronic edition.

termed the fault-normal direction. Pulses aligned in the fault-normal direction of a strike-slip fault can be considered evidence of forward directivity due to the relationship with the shear-wave radiation pattern (Somerville *et al.*, 1997).

DISCUSSION OF THE PULSE CLASSIFICATION RESULTS

Directivity pulses or not?

As mentioned in the Introduction section, it is not straightforward to make assertions about forward directivity being the causal mechanism behind pulse-like waveforms that are classified based solely on the acceleration time series. Be that as it may, some considerations on the origin of the impulsive characteristics can still be interesting; past research indicates

TABLE 1
Summary Information for the Ground Motions Classified as Pulse-Like

Event (yyyy/mm/dd, magnitude)	Station Name	Station Code	Network Code	Epicentral Distance (km)	T_p (s)*	Fault-Normal Pulse†
2019/07/04, M 6.4	Christmas Canyon China Lake	CCC	CI‡	24.4	0.72	—
2019/07/06, M 7.1	Christmas Canyon China Lake	CCC	CI	35.3	3.73	Yes
	Olancha—North Haiwee Reservoir Grounds	43158	CE§	60.0	6.95	Yes
	China Lake	CLC	CI	3.3	4.73	No
	Manuel Prospect Mine	MPM	CI	30.8	6.86	No
	Coso Hot Springs 2	WCS2	CI	31.0	7.45	Yes
	McCloud Flat	WMF	CI	44.0	8.48	Yes
	Volcano Peak 2	WVP2	CI	27.8	7.88	Yes
	Rose Valley Canyon 2	WRV2	CI	37.0	6.78	Yes

*Defined as the pseudo-period of the highest-coefficient wavelet extracted at the orientation with the highest PI score, according to Baker (2007).
†Indicating cases where the highest-PI component falls within 30° of the strike normal (average strike of all segments for the mainshock).
‡Southern California Earthquake Data Center.
§California Strong Motion Instrumentation Program.

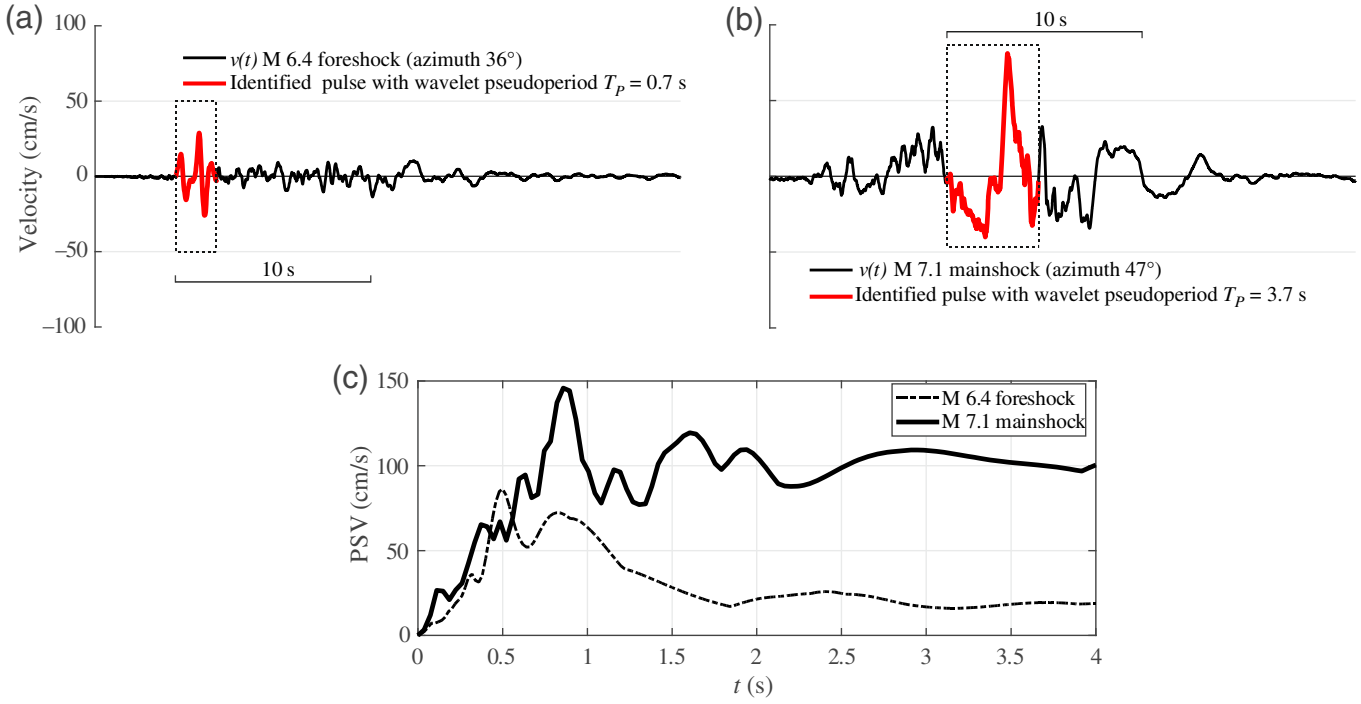

Figure 5. Velocity traces of pulse-like horizontal components recorded at the CCC station during the (a) M 6.4 foreshock and the (b) M 7.1 mainshock; (c) PSV spectra of the two components. The color version of this figure is available only in the electronic edition.

that there may be a difference in the destructive potential between pulse-like ground motions caused by directivity or fling step (Kalkan and Kunnath, 2006), and such distinctions can also be useful when calibrating empirical models for the probability of observing such pulse-like motion under specific site-to-source geometry (Iervolino and Cornell, 2008).

First, it is worth noting that at the CCC station, which is the only station to have recorded a pulse-like signal during the foreshock, an impulsive motion was also detected during the mainshock. Multiple pulse-like motions emerging at a specific site during a sequence has also been observed in the past, for instance, at one of the recording stations in Norcia during the 2016 central Italy sequence (Luzi *et al.*, 2017). Such a recurrence can bring up suspicions that the impulsive behavior may be due to some site-related factor inducing narrowband characteristics in the ground motion, rather than some rupture-related effect. Figure 5 shows the velocity time histories from the two aforementioned CCC records in juxtaposition, both corresponding to orientations exhibiting the respective maximum PI value, which are only 11° from each other and, in the case of the mainshock, in the general fault-normal direction. Also shown are the PSV spectra of the two ground-motion components, as site-specific features can leave a consistent imprint on spectral shape.

The first observation to be made is the notable difference in pulse duration, with T_p being 0.7 s in the first case and 3.7 s in the second. This is not surprising per se, because, as discussed in the following, for directivity-related impulsive motions, T_p is expected to scale with magnitude (Somerville, 2003). By looking at the PSV, and considering that for pulse-like motions, this spectrum is expected to peak at periods T that are, on average, 70% of the wavelet pseudoperiod-based T_p (Baltzopoulos *et al.*, 2016), it can be seen that the only noticeable local spectral amplification shared by the two events is around a period of 0.9 s, which is not related to the observed pulse durations. Finally, it should be noted that during the mainshock, the CCC station was situated at an end-fault location, at least according to this specific finite-fault model, theoretically making it particularly prone to exhibiting directivity effects, a fact that is also confirmed by semiempirical models (Iervolino and Cornell, 2008). Overall, and despite the necessary disclaimers presented at the start, the evidence for the mainshock record leans toward rupture directivity, whereas this is not the case for the foreshock record.

Another noteworthy situation arose at the China Lake (CLC) mainshock record, in which two pulses of significantly different duration were detected along two perpendicular orientations that roughly coincide with the north–south and east–west, as shown in Figure 6. From the figure, it emerges that the most clearly pulse-like component is the north–south one, appearing in Figure 6a. However, neither of the components is oriented close to the fault normal or fault parallel, and the site itself is quite close to the epicenter (3.3 km). This proximity means that this is not a location where one expects the conditions for forward-directivity effects to be easily met, because, contrary to the edge-of-rupture CCC site, only a small part of the rupture has propagated toward the site. On the

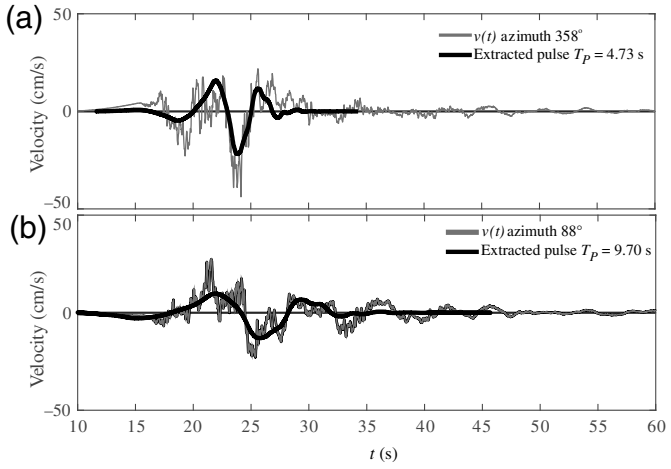

Figure 6. Velocity signals and extracted pulses for two perpendicular horizontal components of the ground motion recorded at the CLC station during the M 7.1 mainshock at azimuths of (a) 358° and (b) 88°.

other hand, most of the slip was concentrated near the hypocenter (Barnhart *et al.*, 2019; Liu *et al.*, 2019), that is, in the vicinity of the CCC site, and there are also hints of fling step affecting the site (to follow). Therefore, there is more than one likely candidate for the causes of this pulse, which might not be directivity related.

Finally, it bears mentioning that there appears to be a relative scarcity of pulse-like records detected among the ground motions from the foreshock. However, it has been suggested that the rupture process in this orthogonal cross-fault may differ from what is typically expected of continuous ruptures propagating along a single fault (Ross *et al.*, 2019). For this reason, one may refrain from comparing this rare situation with what is expected from other, well-studied types of events.

Pulse period

In the literature, there are several empirical models expressing the scaling of pulse period with magnitude, typically based on ordinary least-squares regression (e.g., Mavroeidis and Pacorgiou, 2003; Baker, 2007). According to the model of Chioccarelli and Iervolino (2013), shown here as

$$\ln T_p = -6.19 + 1.07 \cdot M + \varepsilon_{\ln T_p}, \qquad (2)$$

in which $\varepsilon_{\ln T_p}$ is a zero-mean normal variable with a standard deviation of $\sigma_{\ln T_p} = 0.59$, the median T_p for M 6.4 is 1.93 s with a $\pm\sigma_{\ln T_p}$ interval of [1.07 s, 3.48 s], whereas, for M 7.1, the median is 4.08 s and the one-sigma interval being [2.26 s, 7.37 s]. By comparing the pulse periods reported in Table 1 with these statistics, the following considerations emerge: (1) the solitary pulse period observed for the foreshock is unusually low for this magnitude, being below the one-sigma interval; (2) the T_p values found at the southern end-of-fault CCC site and the near-the-epicenter CLC site during the mainshock are close to the median for that magnitude; (3) the pulse-like record sites beyond the northern end of the mainshock rupture all exhibit similar long-period pulses, with durations around one standard deviation above the median prediction. The velocity time histories and extracted pulse waveforms for these ground motions are given in Figure 7. These records, exhibiting T_p values approximately between 7 and 8 s, are examples of the long-period ground motions that can be generated by near-fault directivity, which can impact flexible structures (Koketsu and Miyake, 2008).

Fling step

Another near-source effect that may cause impulsive traits to appear in the ground motion is fling-step, the permanent static offset of the ground near the fault. In fact, extensive surface fault rupture was reported after both the events (Stewart *et al.*, 2019). The static offset calculated by Liu *et al.* (2019) at four stations is shown in Figure 4. For station CLC, it can be observed that the maximum static offset occurred along a direction similar to that of the pulse shown in Figure 6a, which suggests that these impulsive characteristics may have influenced by fling step. Fling-step pulses are theoretically expected to be one sided, but it is not trivial to discern the static from the dynamic part of motion on the velocity trace. In fact, the wavelet that is used for the pulse identification is double sided by construction. This is due to the fact that the PI score was initially oriented toward the detection of directivity pulses. Thus, although an ostensibly fling-step-induced pulse can trigger the algorithm all the same, making the distinction on the origin requires further investigation.

In Figure 8, the velocity traces along the maximum static offset directions (see Fig. 4) are shown for stations CCC, TOW2, and MPM. It is possible that the end-of-fault CCC station is also affected by fling in addition to directivity, as the maximum horizontal static offset reported also occurs at an orientation toward the FN. This could account for the velocity spike visible on an otherwise apparently double-sided pulse (compare with Fig. 5 that shows the same record in the maximum PI orientation instead). It is not obvious if the velocity record at MPM has been influenced by fling step either, as the impulsive waveform appears two sided and scores high on the PI. Therefore, it can be said that both the CCC and MPM stations were found to exhibit impulsive characteristics toward the direction of maximum horizontal static offset, which would hint at fling step, but the pulses do not appear to be one sided, which renders the question inconclusive.

The ground-motion record from station TOW2 was classified as ambiguous, and the velocity time history shown in the figure, reminiscent of slow gradual damping-out of harmonic oscillations, is more likely related to site effects than fling step. This would be consistent with the subsoil classification of the site as D (according to the National Earthquake Hazards Reduction Program), although the site was far from areas known to have been affected by lateral spreading (Stewart *et al.*, 2019).

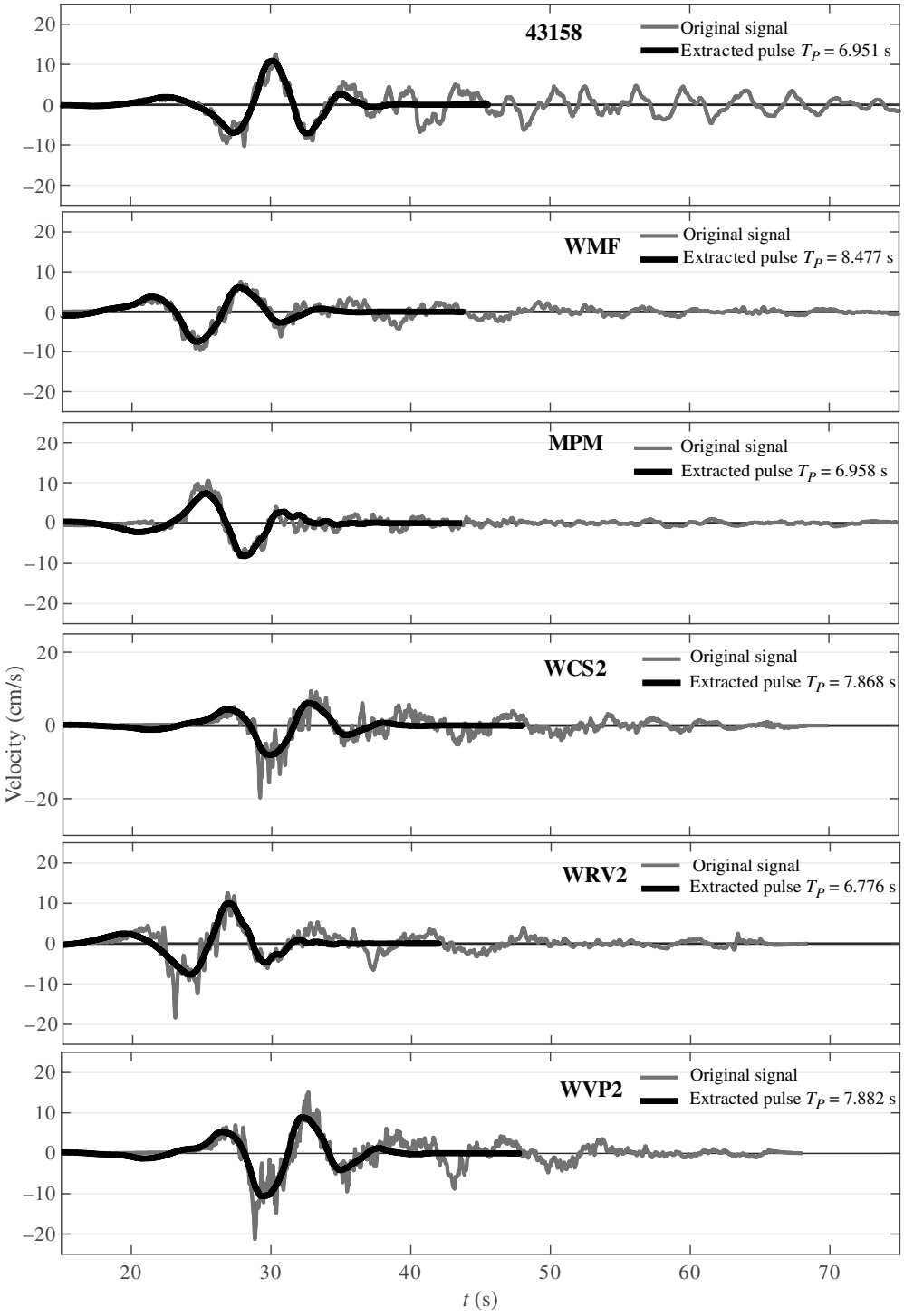

Figure 7. Velocity time histories of the highest PI components of seven stations exhibiting long-duration pulses north of the (mainshock) epicenter and extracted pulses.

Directionality

Near-source ground motion may exhibit polarization, in which shaking intensity is consistently larger along certain orientations with respect to others (Pacor *et al.*, 2018). This so-called directionality is also observed in pulse-like near-source motion, but past research has not claimed systematic correlation of this effect with the impulsive attributes (Shahi and Baker, 2014b). In this study, to visualize directionality effects, the ratio $S_a(T)/S_{a,\mathrm{RotD100}}(T)$ is used, with $S_a(T)$ being the 5% damped spectral pseudoacceleration at a generic orientation of the ground motion, and $S_{a,\mathrm{RotD100}}(T)$ the 100th percentile of the rotated, period-dependent component (Boore, 2010). This ratio is shown on polar plots in Figure 9 for three pulse-like ground motions (CCC, CLC, and WMF), for periods $T = T_p$ and plotted against the corresponding PI score.

The pinched $S_a(T)/S_{a,\mathrm{RotD100}}(T)$ polar plots indicate polarization of spectral ordinates at vibration periods near T_p, at orientations well aligned with the impulsive components, represented by the PI plot. This behavior also persists at most of the other stations not shown here as well. This observation may have implications in near-source probabilistic seismic hazard analysis (Tothong *et al.*, 2007; Chioccarelli and Iervolino, 2013), in which amplification factors are applied to classical ground-motion models for $S_a(T)$, to account for directivity pulses (e.g., Shahi and Baker, 2011). The point is that ground-motion models typically use some definition of $S_a(T)$ that averages the two components of motion, such as geometric mean or rotated median $S_{a,\mathrm{RotD50}}$, just to name a few. On the other hand, it was observed that directivity-induced amplification can be polarized, affecting a higher fractile such as $S_{a,\mathrm{RotD100}}$.

CONCLUSIONS

The present study dealt with analyzing the near-source accelerometric records from the **M** 6.4 foreshock and the **M** 7.1 mainshock of the 2019 Ridgecrest earthquake sequence, in

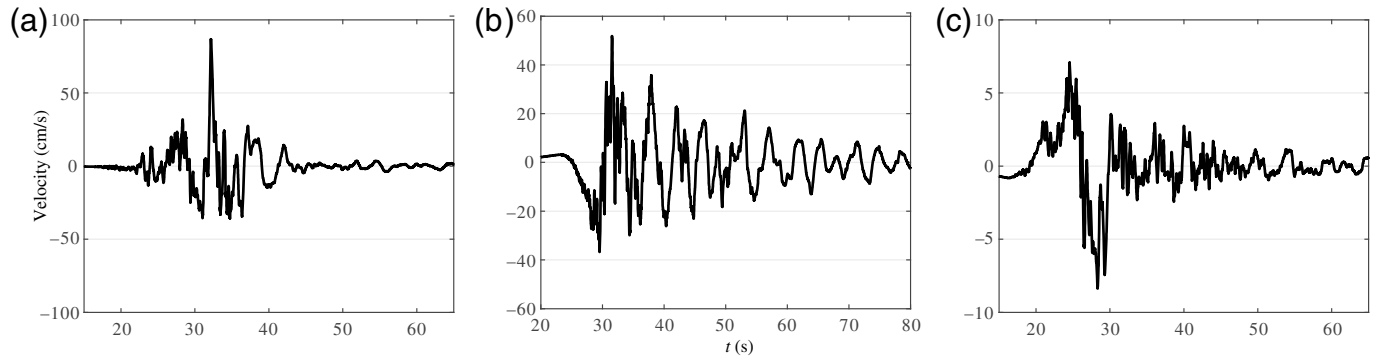

Figure 8. Velocity traces along the direction maximum static offset from the M 7.1 mainshock, recorded at stations (a) CCC, (b) TOW2, and (c) MPM.

search for ground motions exhibiting pulse-like characteristics. This investigation is motivated by the high interest of earthquake engineers in this type of seismic input, due to its elevated damage potential toward structures. Consolidated numerical tools were used to screen the available records, and the final pulse classification was performed manually by visual inspection.

This investigation yielded nine ground motions that were classified as pulse-like, only one belonging to the foreshock. These acceleration records, rotated to the orientation of the maximum PI component, are provided in file S1 of the supplemental material available to this article, adding to available databases of pulse-like ground motions that can be used for dynamic analysis of structures in near-source seismic risk assessment. Examination of the evidence provided by finite-fault geometry, pulse orientations, and comparison with empirical models in the literature led to the conclusion that at least one of the mainshock impulsive motions is probably directivity related. It is possible that some of the other observed pulses are also influenced by fling step, but the evidence is not conclusive on that count. Although these records trigger a positive on the pulse identification algorithm also in the orientation in which the maximum static offset has been reported, the corresponding pulse still appears double sided in that direction, which is what would be expected from directivity-induced impulsive behavior, rather than from fling step. Finally, it was observed that most of the pulse-like ground motions detected exhibited prominent polarization of the spectral ordinates at vibration periods near the pulse period. This polarization was observed toward the orientation of the impulsive component and may have implications in the calibration of corrective factors that are typically applied to ground-motion models, to account for directivity-induced spectral amplification.

DATA AND RESOURCES

The supplemental material contains the acceleration records of the ground motions classified as pulse-like, provided in the compressed file S1, rotated to the orientation of the maximum pulse indicator component and the transverse. Raw ground-acceleration records of

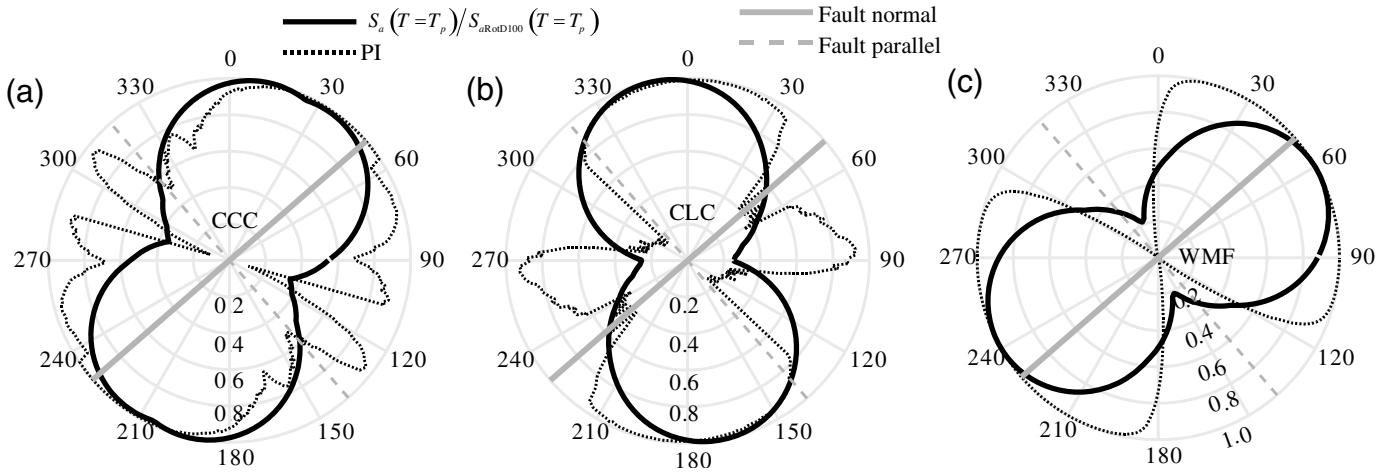

Figure 9. Ratio of the spectral acceleration per orientation to the 100th rotated percentile at period equal to pulse period, plotted against PI score for the pulse-like ground motions recorded during the mainshock at stations (a) CCC, (b) CLC, and (c) WMF.

the Ridgecrest sequence were obtained from the Southern California Seismic Network, the United States National Strong-Motion Network and the California Strong Motion Instrumentation Program (http://service.ncedc.org/, http://service.scedc.caltech.edu/, last accessed December 2019). Information on location and magnitude were taken from the U.S. Geological Survey (USGS, http://earthquake.usgs.gov/, last accessed November 2019). Finite-fault geometry and static offset displacements were obtained from the supplemental material of Liu *et al.* (2019) available at the publisher's website, last accessed January 2020. Corrected ground-acceleration records used for Figure 1 were taken from the NEar-Source Strong-motion flat-file (v1.0) (NESS1) database (http://ness.mi.ingv.it/, last accessed January 2020). MATLAB implementation of the algorithm in Baker (2007) was obtained at the author's personal website, last accessed in 2016. All other software tools used for the preparation of this article were developed by the authors in MATLAB environment. The MATLAB is available in www.mathworks.com/products/matlab (last accessed September 2019).

ACKNOWLEDGMENTS

This study was developed within the activities of the 2019–2021 Department of Civil Protection (DPC)—Rete di Laboratori Universitari d'Ingegneria Sismica (ReLUIS) research project funded by the Italian DPC of the Italian Presidency of the Ministers' Council. The authors would like to acknowledge the two anonymous reviewers, whose observations helped improve the quality of the article.

REFERENCES

Alavi, B., and H. Krawinkler (2004). Behavior of moment-resisting frame structures subjected to near-fault ground motions, *Earthq. Eng. Struct. Dynam.* **33,** no. 6, 687–706, doi: 10.1002/eqe.369.

Baez, J. I., and E. Miranda (2000). Amplification factors to estimate inelastic displacement demands for the design of structures in the near field, *Proc. of 12th World Conf. on Earthquake Engineering*, Vol. 2, Auckland, New Zealand, 30 January–4 February 2000, New Zealand Society for Earthquake Engineering, 1–8.

Baker, J. W. (2007). Quantitative classification of near-fault ground motions using wavelet analysis, *Bull. Seismol. Soc. Am.* **97,** no. 5, 1486–1501, doi: 10.1785/0120060255.

Baltzopoulos, G., E. Chioccarelli, and I. Iervolino (2015). The displacement coefficient method in near-source conditions, *Earthq. Eng. Struct. Dynam.* **44,** no. 7, 1015–1033, doi: 10.1002/eqe.2497.

Baltzopoulos, G., D. Vamvatsikos, and I. Iervolino (2016). Analytical modelling of near-source pulse-like seismic demand for multi-linear backbone oscillators, *Earthq. Eng. Struct. Dynam.* **45,** no. 11, 1797–1815, doi: 10.1002/eqe.2729.

Barnhart, W. D., G. P. Hayes, and R. D. Gold (2019). The July 2019 Ridgecrest, California, earthquake Sequence: Kinematics of slip and stressing in cross-fault ruptures, *Geophys. Res. Lett.* **46,** no. 21, 11,859–11,867, doi: 10.1029/2019GL084741.

Bertero, V. V., S. A. Mahin, and R. A. Herrera (1978). Aseismic design implications of near-fault San Fernando earthquake records, *Earthq. Eng. Struct. Dynam.* **6,** no. 1, 31–42, doi: 10.1002/eqe.4290060105.

Bojórquez, E., and I. Iervolino (2011). Spectral shape proxies and nonlinear structural response, *Soil Dynam. Earthq. Eng.* **31,** no. 7, 996–1008, doi: 10.1016/j.soildyn.2011.03.006.

Bolt, B. (2010). Engineering seismology, in *Earthquake Engineering: From Engineering Seismology to Performance-Based Engineering*, Y. Bozorgnia and V. V. Bertero (Editors), CRC Press, New York, New York, doi: 10.1201/9780203486245.ch2.

Boore, D. M. (2010). Orientation-independent, nongeometric-mean measures of seismic intensity from two horizontal components of motion, *Bull. Seismol. Soc. Am.* **100,** no. 4, 1830–1835, doi: 10.1785/0120090400.

Boore, D. M., and J. J. Bommer (2005). Processing of strong-motion accelerograms: Needs, options and consequences, *Soil Dynam. Earthq. Eng.* **25,** no. 2, 93–115, doi: 10.1016/j.soildyn.2004.10.007.

Bradley, B. A., and M. Cubrinovski (2011). Near-source strong ground motions observed in the 22 February 2011 Christchurch earthquake, *Bull. New Zeal. Soc. Earthq. Eng.* **44,** no. 4, 181–194, doi: 10.5459/bnzsee.44.4.181-194.

Champion, C., and A. Liel (2012). The effect of near-fault directivity on building seismic collapse risk, *Earthq. Eng. Struct. Dynam.* **41,** no. 10, 1391–1409, doi: 10.1002/eqe.1188.

Chioccarelli, E., and I. Iervolino (2010). Near-source seismic demand and pulse-like records: A discussion for L'Aquila earthquake, *Earthq. Eng. Struct. Dynam.* **39,** no. 9, 1039–1062, doi: 10.1002/eqe.987.

Chioccarelli, E., and I. Iervolino (2013). Near-source seismic hazard and design scenarios, *Earthq. Eng. Struct. Dynam.* **42,** no. 4, 603–622, doi: 10.1002/eqe.2232.

Hayden, C. P., J. D. Bray, and N. A. Abrahamson (2014). Selection of near-fault pulse motions, *J. Geotech. Geoenvir. Eng.* **140,** no. 7, 04014030, doi: 10.1061/(ASCE)GT.1943-5606.0001129.

Hough, S. E., E. Thompson, G. A. Parker, R. W. Graves, K. W. Hudnut, T. Dawson, T. Ladinsky, M. Oskin, K. Sirorattanakul, K. Blake, *et al.* (2020). Near-field ground motions from the July 2019 Ridgecrest, California, earthquake sequence, *Seismol. Res. Lett.* **91,** no. 3, 1542–1555, doi: 10.1785/0220190279.

Hutton, L. K., J. Woessner, and E. Hauksson (2010). Seventy-seven years (1932–2009) of earthquake monitoring in Southern California, *Bull. Seismol. Soc. Am.* **100,** no. 2, 423–446, doi: 10.1785/0120090130.

Iervolino, I., and C. A. Cornell (2008). Probability of occurrence of velocity pulses in near-source ground motions, *Bull. Seismol. Soc. Am.* **98,** no. 5, 2262–2277, doi: 10.1785/0120080033.

Iervolino, I., G. Baltzopoulos, and E. Chioccarelli (2016). Preliminary engineering analysis of the august 24th 2016, M_L 6.0 central Italy earthquake records, *Ann. Geophys.* **59,** 1–9, doi: 10.4401/ag-7182.

Kalkan, E., and S. K. Kunnath (2006). Effects of fling step and forward directivity on seismic response of buildings, *Earthq. Spectra* **22,** no. 2, 367–390, doi: 10.1193/1.2192560.

Koketsu, K., and H. Miyake (2008). A seismological overview of long-period ground motion, *J. Seismol.* **12,** no. 2, 133–143, doi: 10.1007/s10950-007-9080-0.

Liu, C., T. Lay, E. E. Brodsky, K. Dascher-Cousineau, and X. Xiong (2019). Coseismic rupture process of the large 2019 Ridgecrest earthquakes from joint inversion of geodetic and seismological observations, *Geophys. Res. Lett.* **46,** no. 21, 11,820–11,829, doi: 10.1029/2019GL084949.

Luzi, L., M. D'Amico, M. Massa, and R. Puglia (2019). Site effects observed in the Norcia intermountain basin (central Italy) exploiting a 20-year monitoring, *Bull. Earthq. Eng.* **17,** no. 1, 97–118, doi: 10.1007/s10518-018-0444-3.

Luzi, L., F. Pacor, R. Puglia, G. Lanzano, C. Felicetta, M. D'Amico, A. Michelini, L. Faenza, V. Lauciani, I. Iervolino, *et al.* (2017). The central Italy seismic sequence between August and December 2016: Analysis of strong-motion observations, *Seismol. Res. Lett.* **88,** no. 5, 1–43, doi: 10.1785/0220170037.

Mavroeidis, G. P., and A. S. Papageorgiou (2003). A mathematical representation of near-fault ground motions, *Bull. Seismol. Soc. Am.* **93,** no. 3, 1099–1131, doi: 10.1785/0120020100.

Pacor, F., C. Felicetta, G. Lanzano, S. Sgobba, R. Puglia, M. D'Amico, E. Russo, G. Baltzopoulos, and I. Iervolino (2018). NESS v1.0: A worldwide collection of strong-motion data to investigate near-source effects, *Seismol. Res. Lett.* **89,** no. 6, 2299–2313, doi: 10.1785/0220180149.

Pacor, F., R. Paolucci, G. Ameri, M. Massa, and R. Puglia (2011). Italian strong motion records in ITACA: Overview and record processing, *Bull. Earthq. Eng.* **9,** no. 6, 1741–1759, doi: 10.1007/s10518-011-9295-x.

Pitarka, A., K. Irikura, T. Iwata, and H. Sekiguchi (1998). Three-dimensional simulation of the near-fault ground motion for the 1995 Hyogo-ken Nanbu (Kobe), Japan, earthquake. *Bull. Seismol. Soc. Am.* **88,** no. 2, 428–440.

Ross, Z. E., B. Idini, Z. Jia, O. L. Stephenson, M. Zhong, X. Wang, Z. Zhan, M. Simons, E. J. Fielding, S. H. Yun, *et al.* (2019). Hierarchical interlocked orthogonal faulting in the 2019 Ridgecrest earthquake sequence, *Science* **366,** no. 6463, 346–351, doi: 10.1126/science.aaz0109.

Shahi, S. K., and J. W. Baker (2011). An empirically calibrated framework for including the effects of near-fault directivity in probabilistic seismic hazard analysis, *Bull. Seismol. Soc. Am.* **101,** no. 2, 742–755, doi: 10.1785/0120100090.

Shahi, S. K., and J. W. Baker (2014a). An efficient algorithm to identify strong-velocity pulses in multicomponent ground motions, *Bull. Seismol. Soc. Am.* **104,** no. 5, 2456–2466, doi: 10.1785/0120130191.

Shahi, S. K., and J. W. Baker (2014b). NGA-West2 models for ground motion directionality, *Earthq. Spectra* **30,** no. 3, 1285–1300, doi: 10.1193/040913EQS097M.

Somerville, P. G. (2003). Magnitude scaling of the near fault rupture directivity pulse, *Phys. Earth Planet. Int.* **137,** no. 1/4, 201–212, doi: 10.1016/S0031-9201(03)00015-3.

Somerville, P. G., N. F. Smith, R. W. Graves, and N. A. Abrahamson (1997). Modification of empirical strong ground motion attenuation relations to include the amplitude and duration effects of rupture directivity, *Seismol. Res. Lett.* **68,** no. 1, 199–222, doi: 10.1785/gssrl.68.1.199.

Stewart, J., and the GEER Team (2019). Preliminary report on engineering and geological effects of the July 2019 Ridgecrest earthquake sequence, *GEER-064*, Geotechnical Extreme Events Reconnaissance Association, doi: 10.18118/G6H66K.

Tang, Y., and J. Zhang (2011). Response spectrum-oriented pulse identification and magnitude scaling of forward directivity pulses in near-fault ground motions, *Soil Dynam. Earthq. Eng.* **31,** no. 1, 59–76, doi: 10.1016/j.soildyn.2010.08.006.

Tinti, E., L. Scognamiglio, A. Michelini, and M. Cocco (2016). Slip heterogeneity and directivity of the M_L 6.0, 2016, Amatrice earthquake estimated with rapid finite-fault inversion, *Geophys. Res. Lett.* **43,** no. 20, 10,745–10,752, doi: 10.1002/2016GL071263.

Tothong, P., and C. A. Cornell (2008). Structural performance assessment under near-source pulse-like ground motions using advanced ground motion intensity measures, *Earthq. Eng. Struct. Dynam.* **37,** no. 7, 1013–1037, doi: 10.1002/eqe.792.

Tothong, P., C. A. Cornell, and J. W. Baker (2007). Explicit directivity-pulse inclusion in probabilistic seismic hazard analysis, *Earthq. Spectra* **23,** no. 4, 867–891, doi: 10.1193/1.2790487.

U.S. Geological Survey (USGS) Earthquake Science Center (1931). *United States National Strong-Motion Network*, International Federation of Digital Seismograph Networks, doi: 10.7914/SN/NP.

Zhai, C., Z. Chang, S. Li, Z. Q. Chen, and L. Xie (2013). Quantitative identification of near-fault pulse-like ground motions based on energy, *Bull. Seismol. Soc. Am.* **103,** no. 5, 2591–2603, doi: 10.1785/0120120320.

Manuscript received 19 January 2020
Published online 9 June 2020